DOI: 10.7251/JEPM2001001D
UDC: 662.612/.613:621.867.2

Journal of
Engineering & Processing Management

ORIGINAL PAPER

3D model of a Monolithic Honeycomb Adsorber for Electric Swing Adsorption for Carbon Dioxide Capture

Marija Ječmenica Dučić[1] | Ivana Đukić[2] | Nikola Nikačević[3] | Menka Petkovska[3]

[1]University of Belgrade, "VINČA" Institute of Nuclear Sciences - National Institute of the Republic of Serbia, Department of Physical Chemistry, 12-14 Mike Alasa, Box 522, 11001 Belgrade, Republic of Serbia

[2]NIS, Pancevo Refinery, 199 Spoljnostarcevacka, 26101 Pancevo, Republic of Serbia

[3]University of Belgrade, Faculty of Technology and Metallurgy, Department of Chemical Engineering, 4 Karnegijeva, 11000 Belgrade, Republic of Serbia

Correspondence
M. Ječmenica Dučić
Email: marija.jecmenica@vin.bg.ac.rs

Abstract

The goal of this work was to develop a 3D model of Electric Swing Adsorption process for carbon dioxide capture from effluent gasses from power plants. Detailed 3D model of the composite honeycomb monolithic adsorber was developed for a single monolith channel and can be used to simulate and represent different physical properties: velocity, concentration and temperature. The advantage of this model is the fact that all physical properties and results can be presented visually in the 3D domain. COMSOL Multiphysics software was used for solving partial differential equations and simulations of adsorption and electrothermal desorption processes. Some simulation results are presented in this work. The results obtained from 3D simulations will be used for the adsorber model reduction to the 1D model which will be used for modeling and optimization of the whole ESA cycle due to its simplicity and computational demands. Simulation and optimization runs based on the 1D model will be performed in g-Proms software.

Keywords: CO_2 capture, electrothermal desorption, COMSOL Multiphysics.

1. INTRODUCTION

Production of electricity and heat is responsible for the major part of the worldwide CO_2 anthropogenic emissions. The generation of electricity from fossil fuels, as well as from natural gas plants is a big source of greenhouse gases emissions and large amounts of carbon dioxide are discharged to atmosphere. Accumulation of greenhouse gases in the atmosphere is directly linked to the increased global warming and climate changes. In order to control the CO_2 emission, investigations in this field has grown into a large world-wide research effort encompassing different capture technologies and knowledge of new materials. The capture techniques can be divided into three groups: post-combustion capture, pre-combustion capture and oxy-fuel combustion capture. The current leading separation process for CO_2 capture from post-combustion flue gases is amine scrubbing (Wang, Zhao, Otto, Robinius, & Stolten 2017; Wu, Yu, Qin, & Zhang 2014). This technology for CO_2 capture presents a series of important disadvantages as the degradation of solvents in the presence of oxygen, high energy demands for solvents regeneration, solvents loss by evaporation and equipment corrosion. Adsorption – based cyclic processes are considered as an important alternative to amine scrubbing for CO_2 capture: Pressure Swing Adsorbtion (PSA), Temperature Swing Adsorption (TSA) and recently, Electric Swing Adsorption (ESA). Pressure Swing Adsorption (PSA) has been intensively studied for CO_2 capture by several research groups (Grande 2012; Kacem, Pellerano, & Delebarre 2015; Riboldi & Bolland 2015; 2017). Vacuum Swing Adsorption (VSA) as a special case of PSA (Cavenati, Grande, & Rodrigues 2006; Rezaei, Mosca, Webley, Hedlund, & Xiao 2010; Webley et al. 2017) Temperature Swing Adsorption (TSA) (Ben-Mansour & Qasem 2018; Jiang et al. 2020; Moate & Levan 2010; Yang et al. 2014), as well as the combination of TSA and PSA (Plaza, García, Rubiera, Pis, & Pevida 2010; Tlili, Grévillot, & Vallières 2009) have been recently tested as well. Electric Swing Adsorption (ESA) represents a variety of Temperature Swing Adsorption, cyclic adsorption based process

in which the regeneration of adsorbent is achieved by increasing its temperature.

The main difference between ESA and TSA is the method to achieve the required regeneration temperature. ESA is a process where heat required for CO_2 desorption is generated by the Joule effect created by passing electricity through a conducting adsorbent. The idea was first presented 50 years ago by Fabuss and Dubois Fabuss and Dubois (1970). Since then many studies have considered different aspects of the concept. Lin and Economy Lin and Economy (1973) proposed the method for the reactivation of activated carbon fibers. Petkovska et al. developed several dynamic models and applied the principle to a bed constituted with parallel layers of activated carbon fiber cloth (Petkovska, Antov, & Sullivan 2005; Petkovska, Antov-Bozalo, Markovic, & Sullivan 2007; Petkovska & Mitrovic 1994; Petkovska & Mitrović 1994; Petkovska, Tondeur, Grevillot, Granger, & Mitrović 1991), while Sullivan et al. used the method for capturing volatile organic compounds from gas streams (Sullivan, Rood, Dombrowski, & Hay 2004 a. 2004; Sullivan, Rood, Grevillot, Wander, & Hay 2004 b; Sullivan, Rood, Hay, & Qi 2001).

Structured adsorbents show several advantages in gas separation processes such as enhanced mass transfer, reduced pressure drop, and improved thermal management. This includes lower energy consumption, higher throughput and superior recovery and purity of products (Rezaei & Webley 2009; 2010). Yu et al. applied the principle on an activated carbon monolith (Cheng et al. 2002; Yu, Luo, & Grevillot 2007; Yu, Luo, & Grévillot 2004) and two groups leaded by Grande (Grande et al. 2006; Grande, Ribeiro, Oliveira, & Rodrigues 2009; Grande, Ribeiro, & Rodrigues 2009; Grande & Rodrigues 2008) and Ribeiro (Ribeiro, Grande, & Rodrigues 2012; 2013; 2014) have intensively researched and employed ESA process for CO_2 capture on various types of monoliths. Considering the heat is electrically generated, the ESA process for CO_2 capture depends on the availability of adsorbents with high CO_2 capacity and selectivity and good electrical conductivity. Satisfying results have been reached with the activated carbon honeycomb monolith as a conductor and the zeolite particles were packed inside the monolith channels (Ribeiro et al. 2013). The specific task of this work is to develop a high fidelity detailed 3D model of the composite honeycomb monolithic adsorber for CO_2 capture from effluent gasses from power plants which will be used for better understanding of the involved phenomena. The operation of one column of the ESA process is a discontinuous process, in which adsorption of CO_2 (and other species) and subsequent desorption occur in cycles. Thus the whole system consists of several columns containing monolithic honeycomb structure of adsorbent material which conducts electricity. In such columns adsorption and desorption operations switch periodically in order to preserve continuous operation of the overall system. Due to the complexity of the 3D model, within this task only one ESA column is modeled, in which adsorption or desorption is taking place.

COMSOL Multiphysics Modeling Software (COMSOL, Inc) is chosen due to its capabilities to effectively simulate complex multi-physical systems in complex geometries and its recently widespread use for simulating adsorption processes (Abouelella, Fateen, & Fouad 2018; Elsayed, Mahmoud, Al-Dadah, Bowen, & Kaialy 2014; Ghasem 2019; Hasani, Ardejani, & Olya 2017). This detailed 3D model of the ESA, dynamically and spatially distributed, is not suitable for optimization studies of an ESA cycle process due to its complexity and long convergence time. For that reason, a spatially dimensionless 1D model of the ESA based on a detailed and rigorous 3D model, will be developed. Based on the results of 3D simulations that will be run under various operational parameters and in this case considered as dynamic experiments, the 1D model parameters related to transport phenomena will be estimated and new correlations will be obtained for the range of key parameters identified in Comsol. Parameters estimations and simulations based on the reduced model will be performed in gProms software (Process Systems Enterprise Limited, London). The 1D model (reduced model) will further be used for optimization studies of the whole ESA cycle which will be performed in several adsorption columns. Optimization studies will be run in gProms software as well.

2. MATERIAL AND METHODS

Model geometry was chosen in such way as to correspond to the monolithic honeycomb adsorbers with square channels. The honeycomb monolith consists of a specified number of parallel channels that, as it was assumed, all exhibit the same behavior as they are exposed to very similar conditions. In that case, only one channel could be considered as a representative and was consequently modeled. Due to symmetry of the channels, to reduce the computational burden, one quarter of the channel was modeled, as presented in Figure 1. As the overall adsorber performance depends on monolitic honeycomb length and number of channels per square inch of the monolith cross section, two different cases were examined. Both modeled monoliths were the lengths L_c of 200 mm, and they are of 200 of cells per square inch (CPSI) and 400 CPSI. Geometry characteristics corresponding to the Figure 1 of the modeled honeycomb monolith with 200 CPSI, are shown in Table 1.

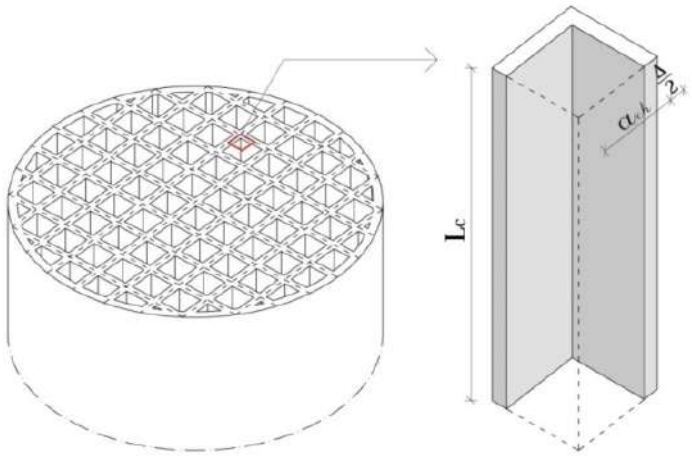

Figure 1. ESA monolith geometry and a detail of the model geometry used for modeling.

Physical characteristics of the monolith wall were estimated based on an assumption that it is an electro conductive composite made of 70% zeolite 13X and 30% carbon. Data for pure zeolite 13X and activated carbon were taken from literature and references are cited in Table 4. It was assumed the adsorption took place only on the zeolite material, while only the carbon material conducted electricity. The electric conductivity of the wall material was taken as 30% of electric conductivity of a carbon monolith, taken from literature (Ribeiro et al. 2013).

Table 1. Geometry characteristics of monolith with 200 CPSI.

Parameter	Value, mm
Monolith length , mm	200
Wall thickness , mm	0.3
Channel width , mm	1.5

2.1. Comsol Multiphysics runs

In the ESA process different physical and chemical phenomena are coupled in a complex geometry. For modeling such specific multi – phenomena application areas in COMSOL Multiphysics Modeling Software (COMSOL, Inc) there is a capability to add different physical effects – modules and to define boundary and initial conditions which describe the model.

The ESA COMSOL model presented in this paper used five different modules: The Reacting Flow (Laminar Flow with mass transfer through boundaries), The Transport of Concentrated Species, Electric Current, Heat Transfer and General Form PDE. The overall modeling domain – a quarter of one monolith channel with the accompanying walls was divided into two subdomains – the monolith channel and the monolith wall.

It should be noticed that the length of the channel is more than 100 times larger than its width. For such cases, the model geometry is usually scaled. Nevertheless, in our model we did not use scaling, as there is no correct way to scale the Navier-Stokes equations in Comsol.

As the length of the channel is more than 100 times larger than its base, a swept mesh in z-direction was used, in order to avoid an enormous number of elements, which would cause excessive memory use and slow convergence. The inlet cross section had been first meshed with sufficiently fine mesh, and then the inlet surface swept mesh with increasing element size along the length was used. The sweeping mesh has the advantage that the user can control the number of element layers and their distribution. The number of the used mesh elements: domain, boundary and edge elements was 13108, 3340 and 371, respectively. An enlarged detail of the used mash is graphically shown in Figure 2.

PARDISO solver (Time dependent solver) was used as we were interested in dynamic response of the system. It gave good results, regarding the model accuracy and computational times used (about 60 minutes). Adsorption isotherms parameters were obtained by non-linear fitting of experimental data in SciLab 5.5.2. Isotherms parameters were optimized by using fminseach function which finds the minimum of the objective function by applying the Nelder – Mead algorithm.

3. THEORETICAL

3.1. Model general assumptions

All monolith channels were considered identical. The monolithic honeycomb structure was represented by one quarter of one channel surrounded with solid composite adsorbent of half wall thickness width. Regarding the

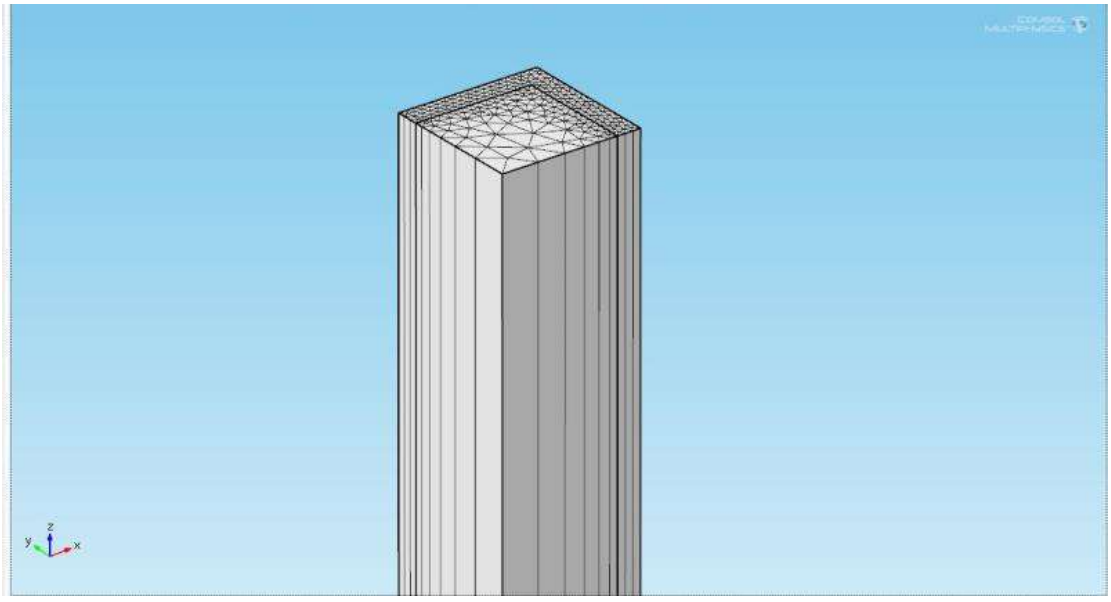

Figure 2. Model geometry and mesh.

fact that only the overall physical, electrical and adsorption characteristics of the solid will be measured in future work, it was assumed that the solid adsorption material is homogeneous, which results in using effective values for the diffusion coefficient, adsorption isotherms, heat capacity and conductivity, electrical resistivity, etc., for the monolith wall. Furthermore, it was assumed that thermal equilibrium is reached within the solid pores. In principle, the model can take into account both the macropore and micropore mass transfer resistance, or assume only macropore diffusion control (by using a large coefficient for mass transfer at the pore surface).

The model took into account that the inlet gas stream consisted of the following components: CO_2, N_2, O_2 and H_2O, according to the boundary conditions for the ESA process, for CO_2 capture from effluent gasses from natural gas power plants. Multicomponent transport of species was modeled, along with competitive Langmuir – type adsorption equilibrium.

$$q_i^* = q_{0,i}\frac{b_i c_{p,i}}{1+\sum_{j=1}^{N} b_j c_p, j} \tag{1}$$

$$q_{0,i} = A_i - \exp\left(B_i \cdot T_s\right) \tag{2}$$

$$b_i = b_{0,i}\exp\left(-\frac{\Delta H_i}{RT_S}\right) \tag{3}$$

It was assumed that the gas was flowing in laminar regime, which is a realistic assumption for dimensions and gas velocities involved in monoliths, behaving ideally in the monolith channel. Regarding the electric resistive heating, simple Ohm's law was considered. Except the heat of adsorption, all physical properties were considered to be temperature dependent, while the pressure gradient across the wall thickness and heat of radiation were neglected.

3.2. Model equations

The model consists of a set of coupled partial differential equations (PDEs) defining the momentum, heat and mass balances for the gas phase in the monolith channel and the mass and heat balances for the monolith wall. In order to define the Joule's heat generated in the monolith wall during desorption, an electric current balance is also included. These PDEs are nonlinear and strongly coupled. Initial and boundary conditions for all PDEs involved in the 3D model are presented in Table 2.

3.2.1. *Momentum balance*

The momentum balance was described by Navier-Stokes equations for compressible fluids. Assumption of the gas flow is in the laminar regime was proven by calculating the Reynolds numbers. The consequent equations are:

$$\rho_g\frac{\partial \bar{v}}{\partial t} + \rho g(\vec{v}\cdot\nabla)\cdot\bar{v} = \nabla\cdot\left[-p_g I + \mu\left(\nabla\dot{v} + (\nabla v)^T - \frac{2}{3}\mu(\nabla\cdot\dot{v^{\cdot}})\,I\right)\right] \tag{4}$$

$$\frac{\partial \rho g}{\partial t} + \nabla\cdot(\rho g\bar{v}) = 0 \tag{5}$$

The boundary conditions defined for equations 1 and 2 corresponded to a velocity driven process, where the velocity at the channel inlet and the pressure at the channel

outlet were defined. The model can be altered to a pressure driven form, where the pressures at both the inlet and outlet can be defined.

3.2.2. *Mass balances*

Owing to the fact that the gas mixture entering and leaving the adsorber cannot be treated as a diluted system, the Maxwell – Stefan approach for multicomponent diffusion was used in the mass balances. The mass balances for the multicomponent gas phase in the monolith channel were defined by the following equations:

$$\frac{\partial\left(\rho_g \omega_i\right)}{\partial t} + \nabla\left(\rho_g \omega_i^{\rho}\right) + \nabla_j^{\rho} = 0 \tag{6}$$

$$\rho_i^{\rho} = -\left(\rho_g D_i^F \nabla\omega_i + \rho_g \omega_i D_i^F \frac{\nabla M}{M}\right) \tag{7}$$

$$D_i^F = \frac{1-\omega_i}{\sum_{k\neq i}^{N} \frac{x_k}{D_{ik}}} \tag{8}$$

$$M = \left(\sum_i \frac{\omega_i}{M_i}\right)^{-1} \tag{9}$$

The mass balances for the multicomponent gas phase in the composite material of the monolith wall were defined by the following equations:

$$\frac{\partial\left(\rho p, g \omega_{p,i}\right)}{\partial t} + \nabla_j^{\rho} p_{p,i} = R_i - \omega_i \sum R_i \tag{10}$$

$$\overset{\mu}{j}_{p,i} = -\left(\rho_g D_{p,i}^F \nabla\omega_{p,i} + \rho_{p,g}\omega_{i,p} D_{p,i} F \frac{\nabla M_p}{M_p}\right) \tag{11}$$

$$D_{p,i}^F = \frac{1-\omega_{p,i}}{\sum_{k\neq i} \frac{x_{p,k}}{D_{p,ik}}} \tag{12}$$

$$M_p = \left(\sum_i \frac{\omega_{p,i}}{M_i}\right)^{-1} \tag{13}$$

The term R_i in equation (10) corresponds to the rate of adsorption of component *i* which is, in turn, defined by the mass flux between the gas and the solid phase in the pores of the monolith wall:

$$R_i = -\frac{1}{\varepsilon}\frac{\partial q_i}{\partial t}\rho_m \tag{14}$$

$$\frac{\partial q_i}{\partial t} = k\left(q_i^* - q_i\right) \tag{15}$$

If the mass transfer coefficient k is set to be very large, the mass transfer resistance on the micropore level will be neglected and local equilibrium within the pores will be obtained. In that case, only the mass transfer resistance on the macropore level will be effective and $D_{p,i}$ will be the overall effective diffusion coefficient for component *i*. Nevertheless, if the diffusion coefficients on both macro and micropore level are known, the mass transfer coefficient k can be evaluated according to the linear driving force theory, and both resistances on the macro and micropore level can be taken into account.

3.2.3. *Energy balances*

The energy balances for the gas phase in the monolith channel and for the composite monolith walls are presented in equations 16 and 17.

$$\rho_g C_{p,g}\frac{\partial T_g}{\partial t} + \rho_g C_{p,g}\vec{v}\nabla T_g = \nabla\left(\lambda_g \nabla T_g\right) \tag{16}$$

$$\rho_m C_{p,m}\frac{\partial T_s}{\partial t} = \nabla\left(\lambda_m \nabla T_s\right) + \sum_i (-\Delta H_i)\frac{\partial q_i}{\partial t}\rho_m + Q_{el} \tag{17}$$

The term Q_{el} defines the Joule's heat generated within the composite wall, when the electricity is turned on. This term is 0 for the adsorption step. During the heating period t_h of the desorption step, it was evaluated through a balance of electricity, which was defined by the following set of equations:

$$Q_{el} = \vec{J}\cdot\vec{E} \tag{18}$$

$$\vec{J} = \sigma\vec{E} \tag{19}$$

$$\vec{E} = -\nabla U \tag{20}$$

3.2.4. *Other equations*

Besides the basic PDEs and their boundary conditions, the ideal gas equation was applied for the gas in the channel and in the wall pores, and the relations between the mass fractions and the gas concentration were also used:

$$\rho_g = \frac{p_g M}{R T_g} \tag{21}$$

$$\rho_{p,g} = \frac{p_{p,g} M_p}{R T_s} \tag{22}$$

$$c_i = \frac{\rho_g \omega_i}{M_i} \tag{23}$$

$$c_{p,i} = \frac{\rho_{p,g}\omega_{p,i}}{M_i} \tag{24}$$

Table 2. Initial and boundary conditions for PDEs involved in the 3D model.

Initial conditions	Boundary conditions					
Momentum balance						
$\vec{u}\|_{t=0,x,y,z} = 0$ $p_g\|_{t=0,x,y,z} = p_g^0$	$\vec{u}\|_{x,y,z=0} = \vec{v}^{\,feed}$	$\vec{u}\|_{x,y=0,z} \hat{n} = 0$	$\vec{u}\|_{x=0,y,z} \hat{n} = 0$	$p_g\|_{x,y,z=L_z} = p_g^{out}$	$\rho_g \vec{u}\|_{x,y=a_{in},z} \hat{n} = \sum \hat{n} \rho N_i$	$\rho_g \vec{u}\|_{x=a_{in},y,z} \hat{n} = \sum \hat{n} \rho N_i$
Mass balance for the multicomponent gas phase in the monolith						
$\omega_i\|_{t=0,x,y,z} = \omega_i^0$	$\omega_i\|_{x,y,z=0} = \omega_i^{feed}$	$\hat{n}\nabla\left(\rho_g \omega_i \vec{u} + \vec{j}_i\right) = 0$	$\hat{n}\nabla\left(\rho_g \omega_i \vec{u} + \vec{j}_i\right)\|_{x=0,y,z} = 0$		$-\hat{n}\rho N_i\|_{x,y=a_{in},z} = N_{0,i}$ $N_{0,i}\|_{x,y=a_{in},z} = K_m(\rho_{p,g}\omega_{p,i} - \rho_g \omega_i)$	$-\hat{n}\rho N_i\|_{x=a_{in},y,z} = N_{0,i}$ $N_{0,i}\|_{x=a_{in},y,z} = K_m(\rho_{p,g}\omega_{p,i} - \rho_g \omega_i)$
Mass balances for the multicomponent gas phase in the composite material of the monolith wall						
$\omega_{p,i}\|_{t=0,x,y,z} = \omega_{p,i}^0$ $q_i\|_{t=0,x,y,z} = q_i^0 = q_i^*$	$-\hat{n}\rho N_i\|_{x,y,z=0} = 0$	$-\hat{n}\rho N_i\|_{x,y=a_{in}+\Delta l/2,z} = 0$	$-\hat{n}\rho N_i\|_{x=a_{in}+\Delta l/2,y,z} = 0$	$\nabla\omega_{p,i}\|_{x,y,z=L_z} = 0$	$-\hat{n}\rho N_i\|_{x,y=a_{in},z} = N_{p0,i}$ $-N_{p0,i}\|_{x,y=a_{in},z} = K_m(\rho_{p,g}\omega_{p,i} - \rho_g \omega_i)$	$-\hat{n}\rho N_i\|_{x=a_{in},y,z} = N_{p0,i}$ $-N_{p0,i}\|_{x=a_{in},y,z} = K_m(\rho_{p,g}\omega_{p,i} - \rho_g \omega_i)$
Energy balance for the gas phase in the monolith channel						
$T_g\|_{t=0,x,y,z} = T_g^0$	$T_g\|_{x,y,z=0} = T_g^{feed}$	$-\hat{n}(\lambda_g \nabla T_g)\|_{x,y=0,z} = 0$	$-\hat{n}(\lambda_g \nabla T_g)\|_{x=0,y,z} = 0$	$\nabla T_g\|_{x,y,z=L_z} = 0$	$-\hat{n}(\lambda_g \nabla T_g)\|_{x,y=a_{in},z} = -K_t(T_g - T_s)$	$-\hat{n}(\lambda_g \nabla T_g)\|_{x=a_{in},y,z} = -K_t(T_g - T_s)$
Energy balance for the composite monolith						
$T_s\|_{t=0,x,y,z} = T_s^0$	$\hat{n}(\lambda_m \nabla T_s)\|_{x,y,z=0} = 0$	$-\hat{n}(\lambda_m \nabla T_s)\|_{x,y=0,z} = 0$	$-\hat{n}(\lambda_m \nabla T_s)\|_{x=0,y,z} = 0$	$\nabla T_s\|_{x,y,z=L_z} = 0$	$-\hat{n}(\lambda_m \nabla T_s)\|_{x,y=a_{in},z} = K_t(T_g - T_s)$	$-\hat{n}(\lambda_m \nabla T_s)\|_{x=a_{in},y,z} = K_t(T_g - T_s)$
Balance of electricity						
$U\|_{t=0,x,y,z} = 0$	$U\|_{x,y,z=0} = \begin{cases} U_0, & 0 < t \le t_h \\ 0, & t > t_h \end{cases}$			$U\|_{x,y,z=L_z} = 0$		

4. RESULTS AND DISCUSSION

4.1. Adsorption isotherms

Because of the temporary lack in experimental data, the isotherms data has been taken from literature. CO_2 adsorption isotherms on zeolite 13X were measured by Lee et al. (2002) and the same group of authors published the water isotherms data (Kim et al. 2003) The N_2 and O_2 adsorption isotherms data were taken from measurements performed by Park, Lee, Moon, Choi, and Lee (2006). All these experimental measurements were performed for adsorption of pure components and the measured data were fitted by single component Langmuir isotherms.

Based on obtained temperature dependent isotherms parameters (Equations 2 and 3), competitive Langmuir isotherms were derived, according to Equation 1. Values of estimated isotherms parameters are shown in Table 3.

The adsorption capacities of the composite adsorbent were adopted as 70% of the corresponding adsorption capacities of pure zeolite 13X. Competitive adsorption isotherms obtained by applied Langmuir model are presented in Figure 3. The model predicts the adsorption capacity of zeolite 13X for CO_2 to be about 7 times higher than for N_2 and O_2 whose quantity adsorbed can be neglected at temperatures higher than 60 °C. Their adsorption is strongly Langmuir and the values of estimated isotherms parameters indicate their similar behavior.

Table 3. Adsorption isotherms parameters used in simulations.

Parameter	CO_2	N_2	O_2	H_2O
b_0, 10^{-6} $m^3 mol^{-1}$	5.52	106	56.6	$5.02 \square 10^{-6}$
$\Delta H, kJ mol^{-1}$	-23.92	-9.30	-9.90	-45.23
A, mol kg^{-1}	5.97	8.28	17.44	33.45
B, mol kg^{-1} K^{-1}	-0.011	-0.022	-0.052	-0.067

4.2. Adsorption and desorption

All simulations were performed in Comsol Multiphysics for honeycomb monoliths with 200 CPSI and 400 CPSI and the geometry presented in Figure 1. The model parameters used in simulations are listed in Table 4. Some

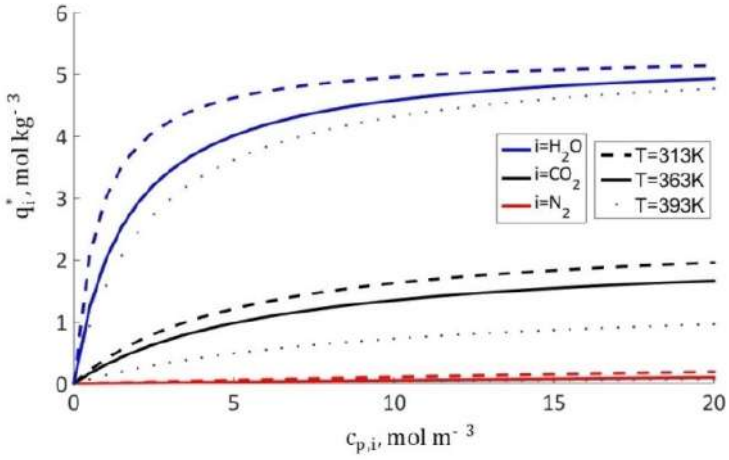

Figure 3. Model predicted CO_2, N_2 and H_2O competitive Langmuir isotherms on temperatures 313 K, 363 K and 393 K.

of the model parameters given in Table 4 are rather arbitrary, as their real values should be obtained from measurements on the real material. The heat and mass transfer coefficients at the gas/wall interface $(K_t and K_m)$ and the mass transfer coefficient at the pore wall (k) were chosen to have large values, in order to simulate the conditions in which no heat and mass transfer resistances were present at these surfaces. For simplicity, the diffusion coefficients of all components were given equal values. This will be changed when realistic data are available. At that stage, the diffusion coefficients in the gas phase will be calculated from appropriate correlations. The dominant resistance to mass transport through composite adsorbent will be experimentally determined and linear driving force parameters will be estimated.

Operating parameters (the initial and inlet conditions for the process variables) are given in Table 5. Simulations were performed for three different inlet gas velocities corresponding to laminar regime of flow in monolithic honeycomb structures. The desorption step was simulated in such a way that at its beginning electrical voltage $\bigcup_o$ was applied to the monolith ends for a short period of time t_h, and then the electricity was turned off, while the flow of gas was continued. The short electrifying period should result in very fast heating of the monolith wall and desorption of CO_2 (and other species in the case of multicomponent adsorption). The initial concentrations of adsorbed species for desorption step were the ones in equilibrium with the gas in the pores of saturated adsorbent.

Solution of the 3D model resulted in concentration and temperature distributions in the monolith channel and monolith wall, as well as pressure and velocity distributions of the gas flowing through the channel, and their change in time. Some of the results of the concentrations, temperatures, pressures and velocities are shown here, in the form of line and 2D surface graphs. 3D graphs which are usually very popular for presentation, are not shown because of the used geometry (more than 100 times larger in the z than in the x and y dimensions) except a magnified detail for concentration of adsorbed CO_2 during adsorption.

Table 4. Model parameters

Parameter	Value	
ε	0.54	
ρ_m, kgm^{-3}	508.4	
K_m, ms^{-1}	10	
$K_t, Wm^{-2}K^{-1}$	10	
k, s^{-1}	10	
$C_{p,g}, Jkg^{-1}K^{-1}$	$1047.64 - 0.37T_g + 9.46 \times 10 - 4T_g^2$	a)
$\lambda_g, Wm^{-1}K^{-1}$	$0.0001T_g + 0.0225$	a)
σ, S^{-1}	$1/(8.95 \times 10^{-4} - 6.95 \times 10^{-7}T_S)$	b)
$C_{p,m}, Jkg^{-1}K^{-1}$	$2.632T_s + 12$	b)
$\lambda_m, Wm^{-1}K^{-1}$	$0.023775 + 0.00014T_s$	c)
$M_{CO_2}, kgmol^{-1}$	0.044	
$M_{NO_2}, kgmol^{-1}$	0.028	
$M_{O_2}, kgmol^{-1}13$	0.032	
$M_{H_2O}, kgmol^{-1}$	0.018	
D_i, m^2s^{-1}	1×10^{-5} $i = CO_2, N_2, H_2O$	
$D_{p,i}, m^2s^{-1}$	9×10^{-9} $i = CO_2, N_2, H_2O$	
$\mu_{p,i}, P\alpha s^{-1}$	$-8.382 * 10^{-7} + -8.357 \times 10^{-8}T_g - 7.694 \times 10^{-11}T_g^2$	a)
$R, Jmol^{-1}K^{-1}$	8.314	

[a)] Ideal gas Taylor polynomials
[b)] Derived from data published by (Ribeiro et al. 2013)
[c)] Derived from data published by (Chan, Chao, & Wu 2015) for zeolite 13X and by (Verma, Nagendra, Kasthurirengan, Shivaprakash, & Behera 2019) for activated carbon.

4.3. Adsorption breakthrough curves

Influence of monolith geometry (number of cells per square inch of monolith cross section) on CO_2 adsorp-

Table 5. Initial and inlet conditions for the processes variables.

Parameter	Value	
	Adsorption	Desorption
υ^{feed}, ms^{-1}	0.011/ 0.022/ 0.055	0.011/ 0.022/ 0.055
υ^{0}, ms^{-1}	0	0
$\omega_{CO_2}^{feed}$	0.0609	0.0609
$\omega_{N_2}^{feed}$	0.8235	0.8235
$\omega_{O_2}^{feed}$	0.1107	0.1107
$\omega_{H_2O}^{feed}$	0.0062	0.0062
$\omega_{CO_2}^{0}$	0	0.0609
$\omega_{N_2}^{0}$	0.8235	0.8235
$\omega_{O_2}^{0}$	0.1765	0.1107
$\omega_{H_2O}^{0}$	0	0.0062
ω_{p,CO_2}^{0}	≈ 0	0.0609
ω_{p,N_2}^{0}	≈ 0	0.8235
ω_{p,O_2}^{0}	≈ 0	0.1107
ω_{p,H_2O}^{0}	≈ 0	0.0062
$q_{CO_2}^{0}, molkg^{-1}$	0	$q_{CO_2}^{*}$
$q_{N_2}^{0}, molkg^{-1}$	$q_{N_2}^{*}$	$q_{N_2}^{*}$
$q_{O_2}^{0}, molkg^{-1}$	$q_{O_2}^{*}$	$q_{O_2}^{*}$
$q_{H_2O}^{0}, molkg^{-1}$	0	$q_{H_2O}^{*}$
T_s^{0}, K^{-1}	313.15	313.15
T_g^{0}, K^{-1}	313.15	313.15
T_g^{feed}, K^{-1}	313.15	313.15
$p_g^{out}, kp\alpha$	111.325	111.325
$p_{p,g}, kp\alpha$	111.325	111.325
$p_g^{0}, kp\alpha$	111.325	111.325
U^{0}, V	0	0
U^{0}, V	0	13/15/17
t_h, s^{-1}	-	10

tion can be observed from Figure 4. The breakthrough curves of the CO_2 adsorption step are shown for two different inlet gas velocities in Figure 4. a), while Figure 4. b) presents the corresponding concentrations of CO_2 adsorbed on the solid phase (the average values in the whole volume of the wall).

As can be seen, CO_2 in the monolith which is of 400 CPSI starts to breakthrough later, and the concentration of CO_2 adsorbed is higher compared to the monolith with 200 CPSI. The influence of gas velocity in the monolith channel on CO_2 adsorption is more obvious from the results shown in Figure 5. The breakthrough curves and corresponding concentrations of CO_2 adsorbed were obtained for monolithic honeycomb structure with 200 CPSI varying the velocity of the inlet feed gas.

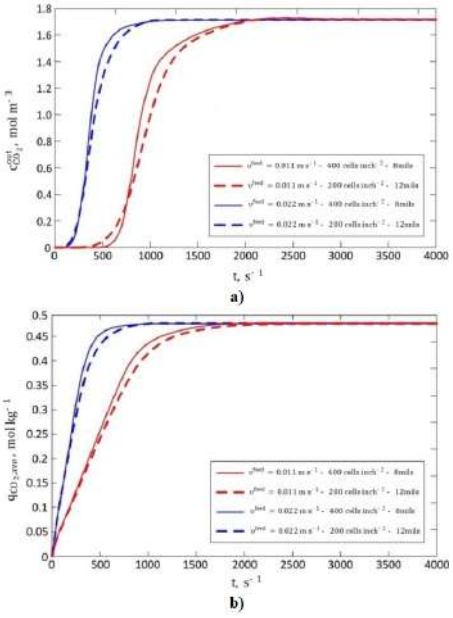

Figure 4. Adsorption curves for monoliths with 200 CPSI and 400 CPSI and inlet gas velocities of 0.011 ms^{-1} and 0.022 ms^{-1}: a) CO_2 concentration at the outlet of the monolith channel, b) averaged CO_2 concentration in monolith wall.

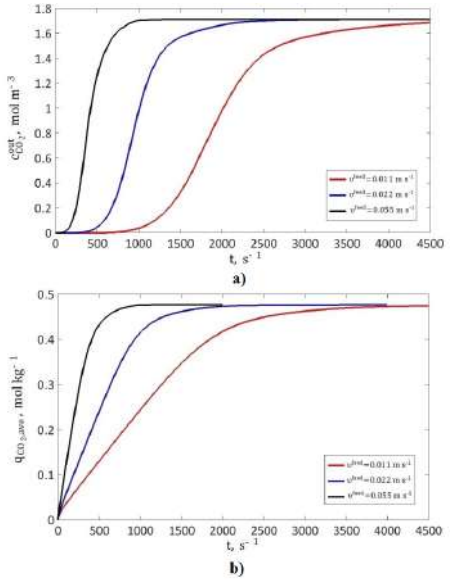

Figure 5. Adsorption curves for inlet gas velocities of 0.011 ms^{-1}, 0.022 ms^{-1} and 0.055 ms^{-1} in monolith with 200 CPSI: a) CO_2 concentration at the outlet of the monolith channel, b) averaged CO_2 concentration in monolith wall.

For the highest velocity the breakthrough occurs at around 150 s. The lower is the velocity, CO_2 starts to break later: three times for gas velocity of 0.022 ms^{-1} and five times for 0.055 ms^{-1}. In order to get a better insight, adsorbed CO_2 concentration distribution after 10 seconds is shown in an enlarged 3D detail in Figure 6. The velocity of feed gas in this simulation was 0.022 ms^{-1}.

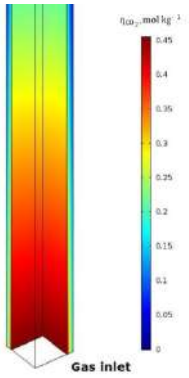

Figure 6. Distribution of adsorbed CO_2 concentrations after 10 seconds adsorbing of flue gas with interstitial velocity of 0.022 m^{-1}.

The influence of the other species present in the feed flue gas on CO_2 adsorption is shown in Figure 7 These simulations were performed for the monolith with 200 CPSI, varying the composition of inlet flue gas while its inlet velocity was uvaried. The CO_2 breakthrough curves and corresponding concentrations of CO_2 adsorbed were compared for adsorption of pure CO_2, mixture of N2 and CO_2 with 6.09 mass% of CO_2, and the feed flue gas whose composition is defined in Table 5.

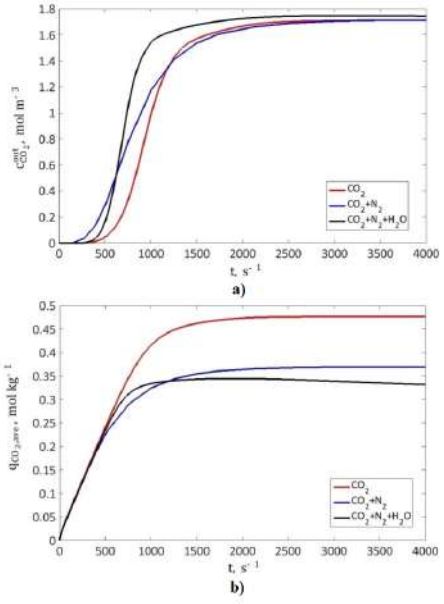

Figure 7. The influence of competitive adsorption - monolith with 200 CPSI and inlet gas velocity of 0.022 ms^{-1}.:
a) CO_2 concentration at the outlet of the monolith channel,
b) averaged CO_2 concentration in monolith wall.

Adsorption of other components decreases maximum adsorption capacity of CO_2 and causes the break earlier. The presence of water is particularly unfavorable for CO_2 adsorption on the composite adsorbent lowering its capacity of CO_2 around 30%.

4.4. Electrothermal desorption

All simulations of electrothermal desorption were performed for the monolithic honeycomb structure which was of 200 CPSI and with the identical electrification period t_h of 10 s. The influence of the voltage applied on CO_2 desorption was simulated varying the voltage (13 V, 15 V and 17 V) while the gas velocity in the monolith channel was unvaried. Figure 8. a) and b) presents the results of simulations in which flue gas inlet velocity was 0.022 ms^{-1}.

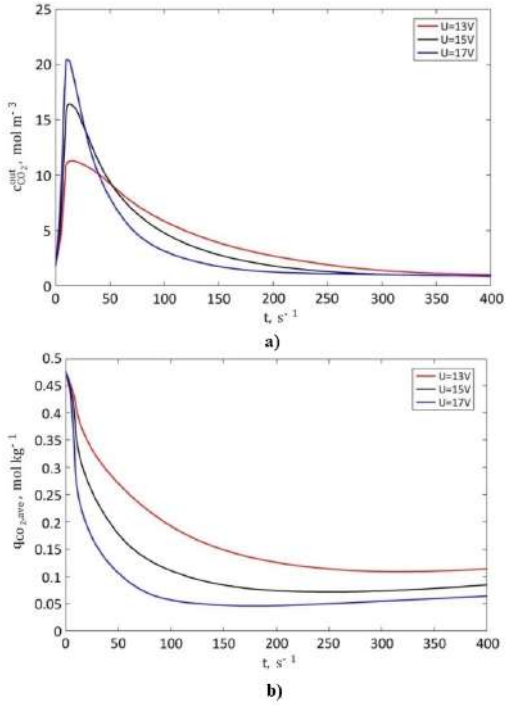

Figure 8. Desorption curves for voltages applied of 13 V, 15 V and 17 V, and inlet gas velocity of 0.022 ms^{-1}:
a) CO_2 concentration at the outlet of the monolith channel,
b) averaged CO_2 concentration in monolith wall

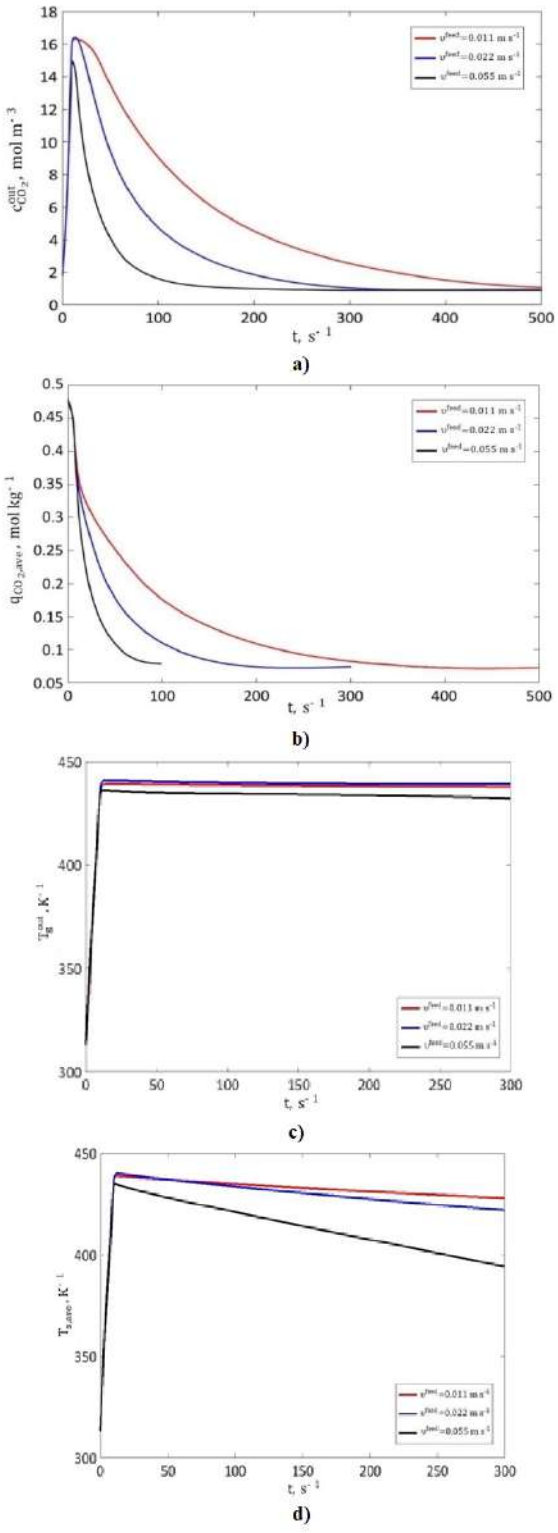

Figure 9. Desorption curves for inlet gas velocities of 0.011 ms^{-1}, 0.022 ms^{-1} and 0.055 ms^{-1}, and voltage applied of 15 V: a) CO_2 concentration at the outlet of the monolith channel, b) averaged CO_2 concentration in monolith wall, c) temperature at the outlet of the monolith channel, d) averaged temperature of the monolith wall.

The higher the voltage applied, the faster the desorption. The adsorbent is fully regenerated after approximately 150 s in the case of the voltage of 17 V, which is 150 % and 200 % faster adsorbent regeneration than the one with lower voltages applied – 225 s for 15 V and 300 s for 13 V. Besides, for the mentioned periods of time, the volume averaged concentration of CO_2 adsorbed is the lowest for the voltage of 17 V, because the adsorbent achieves the highest temperature for the same period of electrification. Gas velocity in the monolith channel should affect both the breakthrough curves (and corresponding concentrations of CO_2 adsorbed) and the temperatures of the gas and the solid phase (monolith wall). The influence was simulated varying velocity, while the voltage applied was unvaried. The results are presented for a voltage of 15 V and three different velocities. Figure 9. a) and b) shows CO_2 breakthrough curves and corresponding concentrations of CO_2 adsorbed. Gas temperature at the outlet of the monolith channel and the average values of the monolith wall temperatures are shown in Figure 9. c) and d).

Inlet gas velocity has no significant effect on the gas temperature at the outlet of the monolith channel, while its influence on monolith wall temperature is obvious even after a short period of time. If the inlet gas velocity was 0.055 ms^{-1}, the adsorbent was fully regenerated after approximately 100 s. It is a 3 times and 5 times shorter regeneration period than if the inlet gas velocities are 0.022 ms^{-1} and 0.011 ms^{-1}, respectively.

4.5. Velocity field and pressure drop

The model also predicted the pressure distribution and the velocity field in the monolith channel and their change in time. Owing to low velocities, the pressure drop establishes a constant pattern in a short time, and has very low values. In Figure 10, pressure drops per adsorber length unit are compared for the honeycomb monoliths that were of 200 CPSI and 400 CPSI.

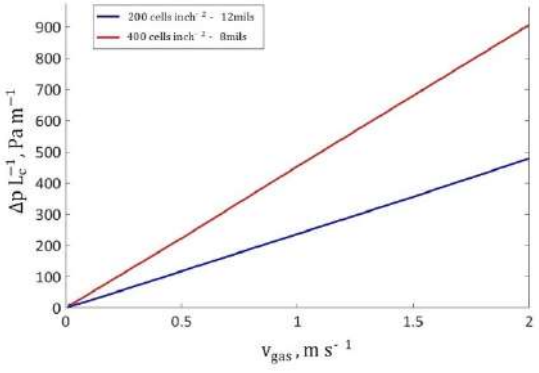

Figure 10. Pressure drops per length unit of honeycomb monoliths with 200 CPSI and 400 CPSI.

The velocity distributions across the monolith cross section at axial position z=100 mm after 500 s of adsorption are shown in Figure 11 below, for two gas velocities used for simulations. The expected hyperbolic velocity profile in the radial direction can be observed. Other simulations results showed the velocity changes in time and axial position are almost negligible, based on which it can be concluded that the velocity profile is established fast and near the channel inlet.

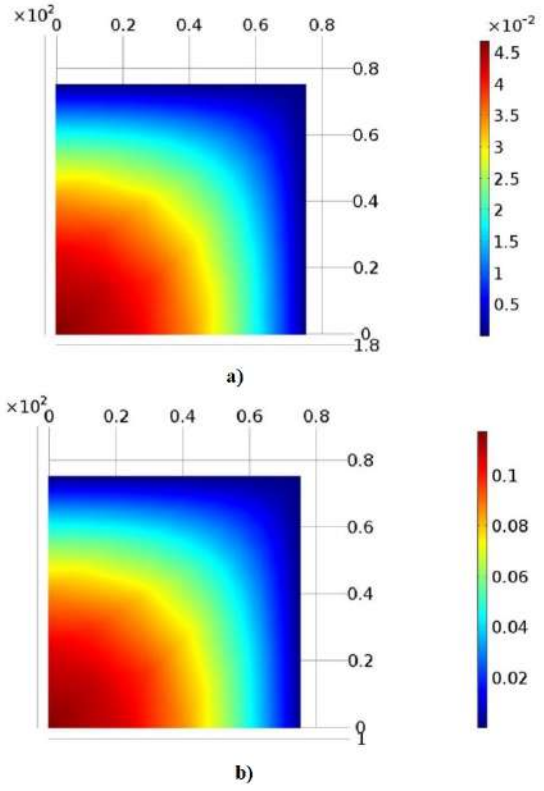

Figure 11. Velocity distribution across monolith cross-section at axial position z=100 mm after 500 s:
a) inlet gas velocity of 0.022 ms^{-1},
b) inlet gas velocity of 0.055 ms^{-1}.

5. CONCLUSIONS

The modeling of the ESA system in COMSOL appeared to be a challenging task, with a number of numerical problems which needed to be surmounted. Finally, those problems were tackled and an operating and robust model which can be used for simulations under different operating conditions is delivered.

The results of performed simulations provided a better understanding of the phenomena involved in the ESA process based on the use of adsorbers with monolithic honeycomb loadings. In addition, several important conclusions for 1D model developing were drawn. As it was expected, the results of CO_2 adsorption simulations showed the CO_2 break is later if the velocity of inlet gas is lower. But the lower the velocity, the slower the regeneration of the adsorbent. Simulations results of CO_2 desorption showed that the higher the voltage applied and the velocity of inlet flue gas, the faster the adsorbent regeneration. It can be concluded that, during desorption, the higher voltage should be applied for shorter periods of time, with higher inlet gas velocities. The CO_2 break was significantly later in the monolith which was of 400 CPSI, but because of the pressure drop, in the 1D model development, only the honeycomb monolith which is of 200 CPSI will be observed. It should be remarked that simulated monolith is the unit of the laboratory range. In the 1D model up to 10 times longer unit will be simulated. Additional simulations will be run for a wider range of inlet gas velocities, keeping the gas flow in laminar regime and pressure drop up to 500 Pa m^{-1}. The results of further 3D simulations will be used for parameters estimation studies based on the 1D model.

Water isotherms and obtained competitive adsorption breakthrough curves point out the necessity of removing H2O from feed flue gas. In the 1D model simulations, the inlet gas will not contain any water, and based on the results of adsorption equilibrium research, N_2 and O_2 will be observed as a single component. New isotherms parameters for CO_2 and N_2 will be obtained by fitting the results of future experimental measurements on a composite zeolite 13X/carbon material.

NOMENCLATURE

- α_{ch}, m - Inner width of the monolith channel
- $A_i, molkg^{-1}$ - Parameter in the temperature dependence for q_{0i}
- $B_i, molkg^{-1}K^{-1}$ - Parameter in the temperature dependence for q_{0i}
- b_i, m^3mol^{-1} - Adsorption equilibrium constant of component i
- b_{0i}, m^3mol^{-1} - Adsorption constant of component i Adsorption constant of component i at limit $\longrightarrow \infty$
- $c_i, molm^3$ - Concentration of component i in the gas phase
- $C_{p,g}, Jkg^{-1}K^{-1}$ - Gas heat capacity of the gas at constant pressure
- $c_{p,i}, molm^3$ - Concentration of component i in the pores of the composite (adsorbent)
- $C_{p,m}, Jkg^{-1}K^{-1}$ - Wall (composite) heat capacity
- D_i, m^2s^{-1} - Molecular diffusion coefficient of component$i$
- $D_{i,k}, m^2s^{-1}$ - Binary diffusion coefficient of components i and k
- $D_{p,i}, m^2s^{-1}$ - Pore diffusivity coefficient of component i

- $D_{p,ik}, m^2s^{-1}$ - Binary pore diffusivity of components i and k
- $\overrightarrow{\epsilon}, Vm^{-1}$ - Electric field
- k, s^{-1} - Film mass transfer coefficient between the gas in pores and the solid phase
- $K_m ms^{-1}$ - Mass transfer coefficient between the wall and the gas in the channel
- $K_t, Wm^{-2}K^{-1}$ - Heat transfer coefficient between the wall and the gas in the channel
- I - Identity matrix
- $\frac{\rho}{j_{p,i}} kgm^{-3}s^{-1}$ - Mass flux of component i in the pores of the monolith wall
- $\overrightarrow{J}, Am^{-2}$ - Electric current density
- L_c, m - Monolith channel length
- $M, kgmol^{-1}$ - Molar mass of the gas mixture in the channel
- $M_i, kgmol^{-1}$ - Molar mass of component i
- $M_p, kgmol^{-1}$ - Molar mass of the gas mixture in the pores of the monolith wall
- $\frac{\rho}{n}$ - Normal vector
- $\frac{\rho}{N_i}, kgm^{-2}s^{-1}$ - Inward mass flux
- $P_g, P\alpha$ - Gas pressure
- $P_{p,g}, P\alpha$ - Pressure of the gas in the pores of the monolith wall
- $Q_{e,l}, Wm^3$ - Heat generated from electric power
- $Q_i, molkg^{-1}$ - Concentration of component i adsorbed in the solid phase
- $Q_i^*, molkg^{-1}$ - Concentration of the adsorbed component i in equilibrium
- $Q_i^0, molkg^{-1}$ - Maximal amount adsorbed of component i
- $R, Jmol^{-1}K^{-1}$ - Universal gas constant
- R_i, kgm^3s^{-1} - Reaction term for component i
- t, s - Time
- T_g, K - Gas phase temperature
- t_h, s - Electric power switch time
- T_s, K - Temperature of the solid phase
- υ, ms^{-1} - Gas velocity in monolith channel
- υ_{gas}, ms^{-1} - Superficial velocity
- U, V - Electric potential
- x, m - Radial coordinate
- x_k - Molar fraction of k-th component in gas phase
- x_{p_k} - Molar fraction of k-th component in gas mixture in the pores of adsorbent
- y, m - Radial coordinate
- z, m - Axial coordinate

Greek Letters

- $(\Delta H_i), Jmol^{-1}$ - Heat of adsorption of component i
- Δm - Monolith wall thickness
- ε - Composite material (monolith wall) porosity
- $\lambda_g, Wm^{-1}K^{-1}$ - Thermal conductivity of the gas phase
- $\lambda_m, Wm^{-1}K^{-1}$ - Thermal conductivity of the solid phase
- $\mu_g, P\alpha s^{-1}$ - Gas viscosity
- μ_g, kgm^{-3} - Gas density
- $\mu_{p,g}, kgm^{-3}$ - Gas density in the pores of solid material
- μ_m, kgm^{-3} - Composite material bulk density
- σ, Sm^{-1} - Electrical conductivity of the monolith wall
- ω_i - Mass fraction of component i in the gas phase in the monolith channel
- $\omega_{p,i}$ - Mass fraction of component i in the gas in pores of the monolith wall

Superscripts

- feed - Channel inlet
- out - Channel outlet
- 0 - Initial value

REFERENCES

Abouelella, D., Fateen, S., & Fouad, M. (2018). Multiscale modeling study of the adsorption of co2 using different capture materials. *Evergreen*, *5*(1), 43–51. https://doi.org/10.5109/1929729

Ben-Mansour, R., & Qasem, N. (2018). An efficient temperature swing adsorption (tsa) process for separating co2 from co2/n2 mixture using mg-mof-74. *Energy Conversion and Management*, *156*, 10–24. https://doi.org/10.1016/j.enconman.2017.11.010

Cavenati, S., Grande, C., & Rodrigues, A. (2006). Removal of carbon dioxide from natural gas by vacuum pressure swing adsorption. *Energy and Fuels*, *20*(6), 2648–2659. https://doi.org/10.1021/ef060119e

Chan, K., Chao, C., & Wu, C. (2015). Measurement of properties and performance prediction of the new mwcnt-embedded zeolite 13x/cacl2 composite adsorbents. *International Journal of Heat and Mass Transfer*, *89*, 308–319. https://doi.org/10.1016/j.ijheatmasstransfer.2015.05.063

Cheng, Z.-M., Yu, F., Grevillot, G., Luo, L., Tondeur, D., & Yuan, W. (2002). Redistribution of adsorbed vocs in activated carbon under electrothermal desorption. *AIChE Journal*, *48*(5), 1132–1138. https://doi.org/10.1002/aic.690480522

Elsayed, A., Mahmoud, S., Al-Dadah, R., Bowen, J., & Kaialy, W. (2014). Experimental and numerical investigation of the effect of pellet size on the adsorption characteristics of activated carbon/ethanol. *Energy Procedia*(0), 2327–2330. https://doi.org/10.1016/j.egypro.2014.11.1195

Fabuss, B., & Dubois, W. (1970). Carbon adsorption-electrodesorption process. In *63rd annual meeting of the air pollution control association*. St. Louis.

Ghasem, N. (2019). Modeling and simulation of co2 absorption enhancement in hollow-fiber membrane contactors using cnt-water-based nanofluids. *Journal of Membrane Science and Research*, *5*(4), 295–302. https://doi.org/10.22079/jmsr.2019.100177.1239

Grande, C. (2012). Advances in pressure swing adsorption for gas separation. *ISRN Chemical Engineering*, 1–13. https://doi.org/10.5402/2012/982934

Grande, C., Cavenati, S., Barcia, P., Hammer, J., Fritz, H., & Rodrigues, A. (2006). Adsorption of propane and propylene in zeolite 4a honeycomb monolith. *Chemical Engineering Science*(10), 3053–3067. https://doi.org/10.1016/j.ces.2005.11.058

Grande, C., Ribeiro, R., Oliveira, E., & Rodrigues, A. (2009). Electric swing adsorption as emerging co2 capture technique. *Energy Procedia*, *1*(1), 1219–1225. https://doi.org/10.1016/j.egypro.2009.01.160

Grande, C., Ribeiro, R., & Rodrigues, A. (2009). Co2 capture from ngcc power stations using electric swing adsorption (esa). *Energy and Fuels*, *23*(b), 2797–2803. https://doi.org/10.1021/ef8010756

Grande, C., & Rodrigues, A. (2008). Electric swing adsorption for co2 removal from flue gases. *International Journal of Greenhouse Gas Control*, *2*(2), 116–124. https://doi.org/10.1016/S1750-5836(07

Hasani, S., Ardejani, F., & Olya, M. (2017). Equilibrium and kinetic studies of azo dye (basic red 18) adsorption onto montmorillonite: Numerical simulation and laboratory experiments. *Korean Journal of Chemical Engineering*, *34*(8), 2265–2274. https://doi.org/10.1007/s11814-017-0110-5

Jiang, L., Wang, R., Gonzalez-Diaz, A., Smallbone, A., Lamidi, R., & Roskilly, A. (2020). Comparative analysis on temperature swing adsorption cycle for carbon capture by using internal heat/mass recovery. *Applied Thermal Engineering*, *169*. https://doi.org/10.1016/j.applthermaleng.2020.114973

Kacem, M., Pellerano, M., & Delebarre, A. (2015). Pressure swing adsorption for co2/n2 and co2/ch4 separation: Comparison between activated carbons and zeolites performances. *Fuel Processing Technology*, *138*, 271–283. https://doi.org/10.1016/j.fuproc.2015.04.032

Kim, J., Lee, C., Kim, W., Lee, J., Kim, J., Suh, J., & Lee, J. (2003). Adsorption equilibria of water vapor on alumina, zeolite 13x, and a zeolite x/activated carbon composite. *Journal of Chemical and Engineering Data*, *48*(1), 137–141. https://doi.org/10.1021/je0201267

Lee, J., Kim, J., Kim, J., Suh, J., Lee, J., & Lee, C. (2002). Adsorption equilibria of co2 on zeolite 13x and zeolite x/activated carbon composite. *Journal of Chemical and Engineering Data*, *47*(5), 1237–1242. https://doi.org/10.1021/je020050e

Lin, R., & Economy, J. (1973). Preparation and properties of activated carbon fibers derived from phenolic precursor. In (Vol. 2, pp. 143–152).

Moate, J., & Levan, M. (2010). Temperature swing adsorption compression: Effects of nonuniform heating on bed efficiency. *Applied Thermal Engineering*, *30*(6-7), 658–663. https://doi.org/10.1016/j.applthermaleng.2009.11.013

Park, Y.-J., Lee, S.-J., Moon, J.-H., Choi, D., & Lee, C. (2006). Adsorption equilibria of o2, n2, and ar on carbon molecular sieve and zeolites 10x, 13x, and lix. *Journal of Chemical Engineering Data*, *51*(3), 1001–1008. https://doi.org/10.1021/je050507v

Petkovska, M., Antov, D., & Sullivan, P. (2005). In *Electrothermal desorption in an annular-radial flow-acfc adsorber-mathematical modeling. 585-590*. https://doi.org/10.1007/s10450-005-5989-1

Petkovska, M., Antov-Bozalo, D., Markovic, A., & Sullivan, P. (2007). Multiphysics modeling of electric-swing adsorption system with in-vessel condensation. *Adsorption*, *13*(3-4), 357–372. https://doi.org/10.1007/s10450-007-9028-2

Petkovska, M., & Mitrovic, M. (1994). One-dimensional, nonadiabatic, microscopic model of electrothermal desorption process dynamics. *Chemical Engineering Research Design*, *72*(6), 713–722.

Petkovska, M., & Mitrović, M. (1994). Microscopic modelling of electrothermal desorption. *The Chemical Engineering Journal and The Biochemical Engineering Journal*, *53*(3), 157–165. https://doi.org/10.1016/0923-0467(92)02768-E

Petkovska, M., Tondeur, D., Grevillot, G., Granger, J., & Mitrović, M. (1991). Temperature-swing gas separation with electrothermal desorption step. *Separation Science and Technology*, *26*(3), 425–444. https://doi.org/10.1080/01496399108050482

Plaza, M., García, S., Rubiera, F., Pis, J., & Pevida, C. (2010). Post-combustion co2 capture with a commercial activated carbon: Comparison of different regeneration strategies. *Chemical Engineering Journal*, *163*(1-2), 41–47. https://doi.org/10.1016/j.cej.2010.07.030

Rezaei, F., Mosca, A., Webley, P., Hedlund, J., & Xiao, P. (2010). Comparison of traditional and structured adsorbents for co2 separation by vacuum-swing adsorption. *Industrial and Engineering Chemistry Research*, *49*(10), 4832–4841. https://doi.org/10.1021/ie9016545

Rezaei, F., & Webley, P. (2009). Optimum structured adsorbents for gas separation processes. *Chemical Engineering Science*, *64*(24), 5182–5191. https://doi.org/10.1016/j.ces.2009.08.029

Rezaei, F., & Webley, P. (2010). Structured adsorbents in gas separation processes. *Separation and Purification Technology*, *70*(3), 243–256. https://doi.org/10.1016/j.seppur.2009.10.004

Ribeiro, R., Grande, C., & Rodrigues, A. (2012). Electrothermal performance of an activated carbon honeycomb monolith. *Chemical Engineering Research and Design*, *90*(11), 2013–2022. https://doi.org/10.1016/j.cherd.2012.03.010

Ribeiro, R., Grande, C., & Rodrigues, A. (2013). Activated carbon honeycomb monolith-zeolite 13x hybrid system to capture co2 from flue gases employing electric swing adsorption. *Chemical Engineering Science*, *104*, 304–318. https://doi.org/10.1016/j.ces.2013.09.011

Ribeiro, R., Grande, C., & Rodrigues, A. (2014). Electric swing adsorption for gas separation and purification: A review. *Separation Science and Technology*, *49*(13), 1985–2002. https://doi.org/10.1080/01496395.2014.915854

Riboldi, L., & Bolland, O. (2015). Evaluating pressure swing adsorption as a co2 separation technique in coal-fired power plants. *International Journal of Greenhouse Gas Control*, *39*, 1–16. https://doi.org/10.1016/j.ijggc.2015.02.001

Riboldi, L., & Bolland, O. (2017). Overview on pressure swing adsorption (psa) as co2 capture technology: State-of-the-art, limits and potentials. *Energy Procedia*, *114*, 2390–2400. https://doi.org/10.1016/j.egypro.2017.03.1385

Sullivan, P., Rood, M., Dombrowski, K., & Hay, K. (2004 a. 2004). Capture of organic vapors using adsorption and electrothermal regeneration. *Journal of Environmental Engineering*, *130*(3), 3–258.

Sullivan, P., Rood, M., Grevillot, G., Wander, J., & Hay, K. (2004 b). Activated carbon fiber cloth electrothermal swing adsorption system. *Environmental Science and Technology*, *38*(18), 4865–4877. https://doi.org/10.1021/es0306415

Sullivan, P., Rood, M., Hay, K., & Qi, S. (2001). Adsorption and electrothermal desorption of hazardous organic vapors. *Journal of Environmental Engineering*, *127*(3), 733–9372.

Tlili, N., Grévillot, G., & Vallières, C. (2009). Carbon dioxide capture and recovery by means of tsa and/or vsa. *International Journal of Greenhouse Gas Control*, *3*(5), 519–527. https://doi.org/10.1016/j.ijggc.2009.04.005

Verma, R., Nagendra, H., Kasthurirengan, S., Shivaprakash, N., & Behera, U. (2019).
In *Thermal conductivity studies on activated carbon based cryopanel* (Vol. 502). https://doi.org/10.1088/1757-899x/502/1/012197

Wang, Y., Zhao, L., Otto, A., Robinius, M., & Stolten, D. (2017). A review of post-combustion co2 capture technologies from coal-fired power plants. *Energy Procedia*, *114*, 650–665. https://doi.org/10.1016/j.egypro.2017.03.1209

Webley, P., Qader, A., Ntiamoah, A., Ling, J., Xiao, P., & Zhai, Y. (2017). A new multi-bed vacuum swing adsorption cycle for co2 capture from flue gas streams. *Energy Procedia*, *114*, 2467–2480. https://doi.org/10.1016/j.egypro.2017.03.1398

Wu, X., Yu, Y., Qin, Z., & Zhang, Z. (2014). The advances of post-combustion co2 capture with chemical solvents: Review and guidelines. *Energy Procedia*, *63*, 1339–1346. https://doi.org/10.1016/j.egypro.2014.11.143

Yang, M., Chen, N., Huang, C., Shen, Y., Yang, H., & Chou, C. (2014). Temperature swing adsorption process for co2 capture using polyaniline solid sorbent. *Energy Procedia*, *63*, 2351–2358. https://doi.org/10.1016/j.egypro.2014.11.256

Yu, F., Luo, L., & Grevillot, G. (2007). Electrothermal swing adsorption of toluene on an activated carbon monolith. experiments and parametric theoretical study. *Chemical Engineering and Processing*, *46*(1), 70–81. https://doi.org/10.1016/j.cep.2006.04.008

Yu, F., Luo, L., & Grévillot, G. (2004). Electrothermal desorption using joule effect on an activated carbon monolith. *Journal of Environmental Engineering*, *130*(3), 733–9372.